Nanoscale

PAPER

Published on 16 July 2026
Licence and permissions

Cite this: DOI: 10.1039/d6nr01419d

Microdroplets as ambient 'hydrothermal' reactors

Anand Narayanan,[a] Anubhav Mahapatra,[a] Sonali Seth,[a] Sinchan Mukhopadhyay,[a] Soham Chowdhury,[a] Prakrati Patidar,[a] Depanjan Sarkar *[a,b] and Thalappil Pradeep *[a,b,c]

Received 10th April 2026,
Accepted 9th July 2026

DOI: 10.1039/d6nr01419d

rsc.li/nanoscale

Microdroplet reactors offer a unique platform for driving chemical transformations under ambient conditions, mimicking key features of hydrothermal environments. Here, we report a microdroplet-enabled strategy for the room-temperature synthesis of phase-pure, porous, flower-like tenorite (CuO) nanostructures from copper acetate monohydrate *via* a copper hydroxide acetate monohydrate intermediate. Ultrasonic nebulization of homogeneous ethanol–water solutions of copper acetate monohydrate creates confined microenvironments with rapid solvent evaporation and steep concentration gradients, enabling nucleation and growth pathways analogous to hydrothermal systems under ambient conditions, effectively resulting in an "ambient hydrothermal" reaction. The resulting CuO exhibits exceptional functional performance, achieving rapid U(VI) removal from 1000 ppb to below 10 ppb within 5 minutes; over 20-fold higher efficiency than commercial CuO, while retaining structural integrity. This gram-scale, energy-efficient synthesis eliminates high-temperature calcination and demonstrates the broader potential of microdroplets as "ambient hydrothermal" reactors. The method provides a scalable, surfactant-free route to complex oxide nanostructures, bridging the gap between solution-phase and solid-state approaches.

Introduction

Microdroplets have emerged as powerful platforms for transforming materials.[1] Various nanomaterials have been synthesised in microdroplets, exploiting the unique conditions present there.[2–16] These nonequilibrium environments enable green mechanosynthesis of nanoparticles, 2D materials, and hierarchical oxides, assisted by intense electric fields ($\sim 10^9$ V m^{-1}), electrostatic stress, and supersaturation gradients that mimic high-pressure conditions, without external heating or additional chemical reagents.[17–20]

Hydrothermal synthesis (HS) is a process in which precursor materials are thermally treated in a solvent at temperatures above the solvent's normal boiling point inside a sealed pressure vessel, leading to the formation of solid-state products. Conventional HS of CuO is typically carried out at elevated temperatures (usually around 250 °C) and under autogenous pressure to promote dehydration and crystallization from copper-based precursors, such as copper acetate.[21–23] Alternatively, tenorite can also be produced *via* solid-state synthesis, which relies on high-temperature (400–900 °C) thermal decomposition or solid-phase reactions of copper precursors under ambient pressure, offering a simple yet energy-intensive route compared to hydrothermal processing.[24] These energy-intensive methods yield sintered products with limited porosity, hindering their use in adsorption and catalysis applications. Here, we demonstrate that nebulized microdroplets serve as ambient 'hydrothermal' reactors, transforming copper acetate stepwise *via* a copper hydroxide acetate monohydrate intermediate into phase-pure, porous nanoscale tenorite under ambient conditions. Our microdroplet synthesis offers unmatched sustainability advantages: ambient temperatures eliminate energy-intensive heating, water-based nebulization minimizes chemical footprint, and gram-scale scalability supports industrial green chemistry without specialized equipment or pressure vessels. The resulting CuO exhibits rapid U(VI) adsorption, superior to commercial benchmarks, revealing droplet-directed phase control as a scalable route to functional nanomaterials for environmental remediation.

Results and discussion

Ambient 'hydrothermal' synthesis of CuO

The ultrasonic nebulization-assisted transformation of copper acetate monohydrate to tenorite (CuO) is schematically illustrated in Fig. 1. A detailed description of the experimental procedure is provided in the SI. Briefly, copper acetate monohy-

[a]*DST Unit of Nanoscience (DST UNS) & Thematic Unit of Excellence (TUE), Department of Chemistry, Indian Institute of Technology Madras (IITM), Chennai 600036, India. E-mail: depanjan_coe@icsrpis.iitm.ac.in, pradeep@iitm.ac.in*
[b]*Centre of Excellence on Molecular Materials and Functions, Department of Chemistry, Indian Institute of Technology Madras (IITM), Chennai 600036, India*
[c]*International Centre for Clean Water, 2nd Floor, B-Block, IIT Madras Research Park, Kanagam Road, Taramani, Chennai 600113, India*

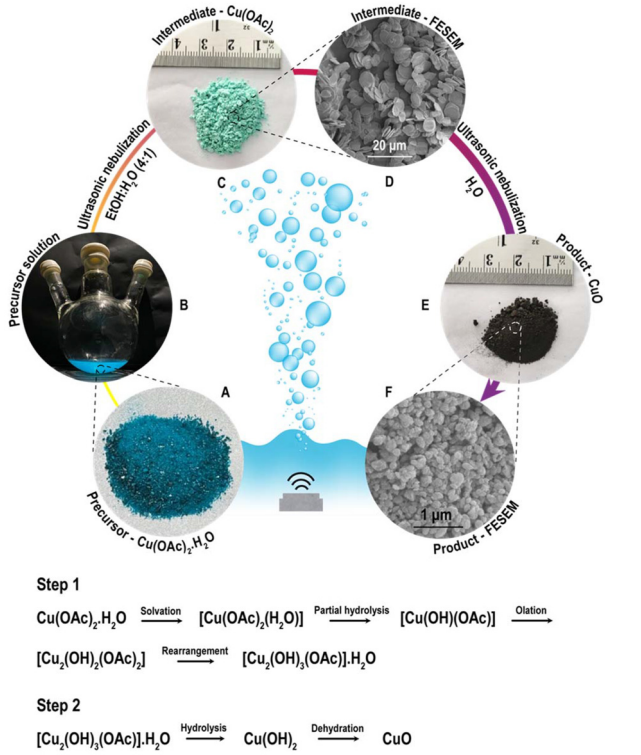

Fig. 1 Schematic of ultrasonic nebulization-assisted transformation of copper acetate monohydrate to CuO. (A) Optical image of solid copper acetate monohydrate precursor. (B) Dissolution in ethanol–water (4 : 1 v/v), forming solvated copper acetate species. (C) Optical image of copper hydroxide acetate monohydrate intermediate (a ruler is to show the scale). (D) FESEM image showing disk-like morphology of the intermediate. (E) Optical image of phase-pure CuO powder. (F) FESEM image revealing nanostructured, porous CuO morphology. Step 1 and 2 of the reaction mechanism are shown at the bottom of the figure.

drate (Fig. 1A) was dissolved in an ethanol–water mixture (4 : 1 v/v) to form a clear solution (Fig. 1B) containing solvated copper acetate. The solution was then subjected to ultrasonic nebulization for 6 h. During this process, micron- to submicron-sized droplets were generated, serving as confined microreactors. Fig. S1 demonstrates an optical photograph of the experimental setup. Rapid solvent evaporation and local concentration gradients within these droplets promoted partial hydrolysis of acetate ligands and rearrangement of copper coordination environments (reaction pathway is schematically shown in Fig. 1, bottom part, step 1), leading to the formation of a blueish-green precipitate (Fig. 1C). The precipitate was separated by centrifugation, thoroughly washed with water and ethanol to remove unreacted precursors, and dried in air. Field-emission scanning electron microscopy (FESEM) revealed uniform disk-like particles (Fig. 1D and Fig. S2). Solvent composition effects were investigated using ethanol–water ratios of 4 : 1 (Fig. S2), 1 : 1 (Fig. S3A), and 2 : 1 (Fig. S3B). The 4 : 1 ratio yielded the most uniform disc-like morphologies, and this ratio was chosen for subsequent experiments. Phase identification by powder X-ray diffraction (PXRD) confirmed the material as copper hydroxide acetate monohydrate (Fig. S4). X-ray photoelectron spectroscopy (XPS) further verified the presence of Cu(II) species (Fig. S5). Further details on solvent screening, control experiments, and the proposed formation mechanism are provided in the later part of the manuscript. During handling, it was observed that the bluish-green precipitate gradually turned blackish-brown upon slight activation, such as gentle sonication. This colour change suggested that the initial precipitate was a metastable intermediate, rather than a thermodynamically stable phase. Therefore, the obtained solid precipitate was subjected to an additional 3 h of ultrasonic nebulization in water (the proposed mechanism is illustrated in Fig. 1, bottom part, step 2). At the end of this process, a blackish-brown precipitate was obtained (Fig. 1E). FESEM imaging revealed that the initially uniform disk-like morphology had transformed into highly porous, flower-like structures with diameters of 300–500 nm (Fig. 1F). This phase was stable and exhibited intriguing nanostructural features, prompting us to investigate it further in subsequent experiments.

Microscopic and spectroscopic characterization

The morphology and structural evolution of the synthesized material were examined by FESEM, as presented in Fig. 2A–C. The low-magnification image (Fig. 2A) reveals a hierarchical assembly composed of porous nanostructures. In contrast, the higher-magnification images (Fig. 2B and C) reveal a well-defined, flower-like architecture composed of interwoven nanosheets.

The phase purity and crystallographic structure of the final product were further investigated by PXRD (Fig. 2D).[25] The diffraction peaks can be indexed fully to monoclinic CuO, confirming the successful conversion of the precursor to crystalline copper oxide under ambient conditions, with no detectable secondary phases. The presence of sharp, intense diffraction peaks indicates the material's highly crystalline nature. To gain insight into the bonding evolution during the transformation, Fourier-transform infrared (FTIR) spectra were recorded in attenuated total reflectance (ATR) mode and compared for the precursor, intermediate, and final products (Fig. 2E). The precursor exhibits a broad O–H stretching band around 3500 cm^{-1}, along with characteristic asymmetric and symmetric stretching vibrations of the acetate group [$\nu_{as}(COO^-)$ and $\nu_s(COO^-)$] located near 1550 and 1400 cm^{-1}, respectively. These acetate-related bands gradually decrease in intensity during the intermediate stage, and they vanish almost completely in the final product, evidencing the removal of acetate ligands. Simultaneously, a strong absorption band emerges near 490 cm^{-1}, corresponding to Cu–O lattice stretching, confirming the formation of CuO and consistent with the PXRD observations. XPS analysis (Fig. 2F) was carried out to elucidate the oxidation state and surface chemical composition of the obtained material. The Cu $2p_{3/2}$ and Cu $2p_{1/2}$ peaks, centered at 933.7 eV and 953.6 eV, respectively, accompanied by two distinct satellite peaks, confirm the presence of Cu(II) species and validate the formation of tenorite. The complete XPS survey spectrum of the synthesized material is shown in Fig. S6.

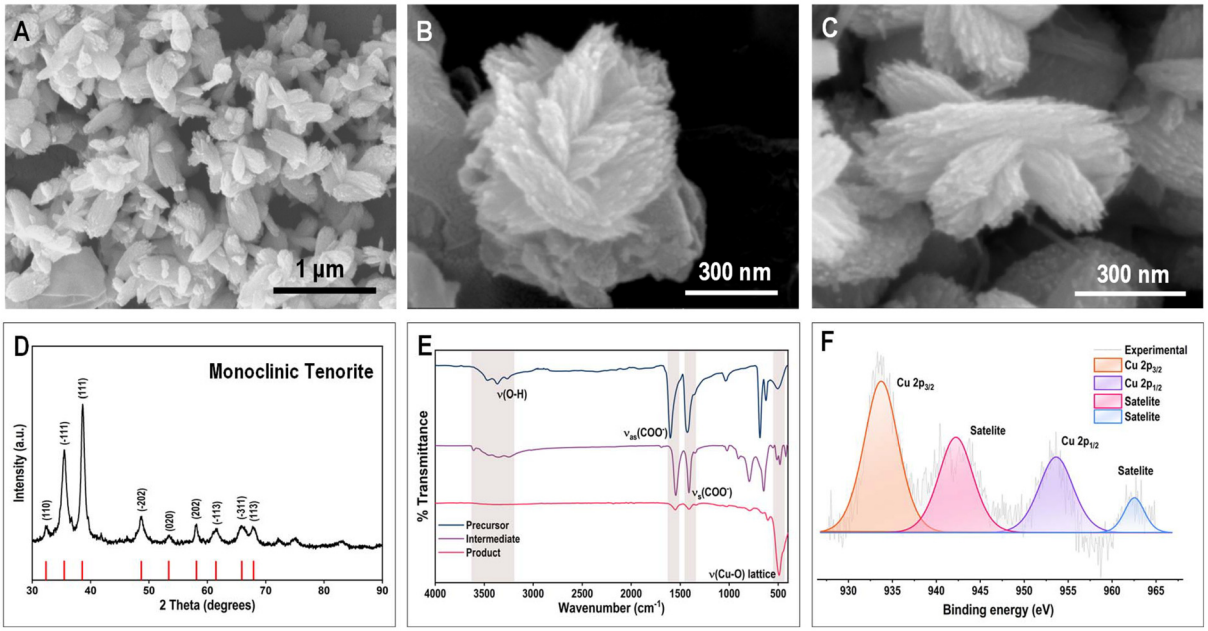

Fig. 2 Structural and spectroscopic characterization of the synthesized CuO. (A) Large area FESEM image showing hierarchical assemblies. (B and C) High-magnification FESEM images revealing the porous flower-like morphology composed of nanosheet subunits. (D) PXRD pattern indexed to monoclinic CuO. (E) ATR-IR spectra of the precursor, intermediate, and final CuO product. (F) XPS profile of Cu showing the Cu $2p_{3/2}$ and Cu $2p_{1/2}$ peaks with characteristic satellite features.

The porous nanostructural characteristics of the as-synthesized tenorite were further examined by high-resolution transmission electron microscopy (HRTEM) and scanning transmission electron microscopy (STEM), as shown in Fig. 3. The TEM image (Fig. 3A) reveals hierarchical, flower-like assemblies composed of interconnected nanosheets, consistent with the morphology observed in the FESEM images. The HRTEM image (Fig. 3B) displays well-resolved lattice fringes with an interplanar spacing of 0.25 nm, corresponding to the (111) plane of monoclinic CuO, in agreement with the PXRD results. The high-angle annular dark-field scanning transmission electron microscopy (HAADF-STEM) image (Fig. 3C) exhibits distinct *Z*-contrast, highlighting the Cu-rich framework of the hierarchical structures and confirming a uniform mass distribution across the particles. Elemental mapping obtained from TEM-energy-dispersive X-ray spectroscopy (TEM-EDS) further verifies that the flower-like architectures are composed exclusively of copper and oxygen (Fig. 3D and E). The corresponding EDS spectrum (Fig. 3F) shows characteristic peaks of Cu and O as the major elemental constituents. At the same time, minor signals from carbon and nickel are attributed to the carbon-coated nickel TEM grid used as the support. The combined microscopic and spectroscopic analyses provide a coherent picture of the stepwise transformation from copper acetate monohydrate to crystalline CuO through an intermediate hydroxide acetate phase. The observed morphological evolution, from disk-like assemblies to porous, flower-like architectures, is intricately related to the physicochemical dynamics within the ultrasonic nebulization environment. The microdroplets act as room-temperature 'hydrothermal' reactors, where solvent evaporation, concentration gradients, and cavitation-generated microjets collectively facilitate anisotropic growth and self-assembly.

To evaluate the broader applicability of the microdroplet-assisted synthesis strategy, the methodology was extended to silver- and zinc-based systems with slight modifications in solvent composition. For the silver precursor, a water-rich medium containing 19 mL of water and 1 mL of ethanol was used, which promoted hydrolysis within the microdroplets and led to the formation of Ag_2O. In contrast, when the zinc precursor was processed in pure ethanol (20 mL), the reduced water content likely limited hydrolysis, favoring the formation of a zinc hydroxy-acetate intermediate phase. The phase compositions of the products were analyzed by XRD, and the corresponding patterns are provided in the SI (Fig. S7 and S8). These results demonstrate that the microdroplet-assisted approach can be extended beyond the CuO system and can yield distinct products through simple adjustment of the reaction medium.

Thermal stability of intermediate and final product

Thermogravimetric analysis (TGA) was conducted on both the intermediate and the final product (Fig. S9). The TGA curve of the intermediate, copper hydroxide acetate monohydrate, shows multiple weight-loss steps: (i) a loss around 130 °C attributed to the removal of adsorbed water; (ii) a weight loss near 200 °C associated with dehydroxylation of the copper hydroxide layers, and (iii) a further decrease around 250 °C

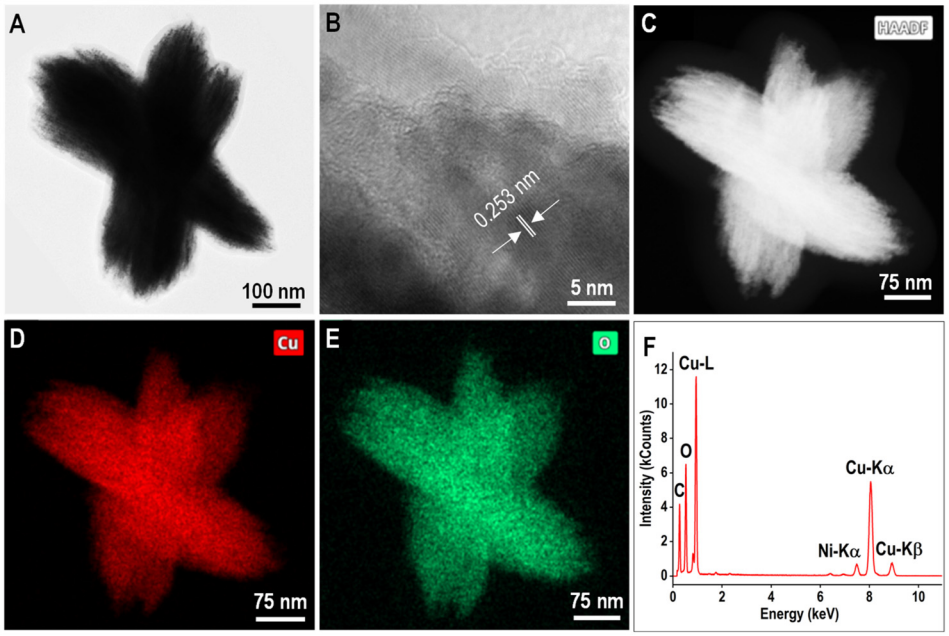

Fig. 3 Transmission electron microscopy (TEM) characterization of the synthesized CuO. (A) TEM image is showing hierarchical morphology. (B) High-resolution TEM (HRTEM) image presents lattice fringes with an interplanar spacing of 0.253 nm corresponding to the (111) plane of monoclinic CuO. (C) High-angle annular dark-field scanning TEM (HAADF-STEM) image. (D and E) Elemental maps of copper and oxygen, respectively, confirming uniform elemental distribution. (F) Energy-dispersive X-ray spectroscopy (EDS) spectrum verifying the presence of Cu and O elements, in the expected ratio (Ni is due to the TEM grid).

corresponding to decomposition of the acetate groups. In contrast, the final product, tenorite, exhibits only a minor weight loss in the 250–300 °C range, which can be assigned to the removal of physically adsorbed moisture and trace surface species, indicating enhanced thermal stability after conversion.

Solvent effects and formation mechanism of the disc-like intermediate

Ultrasonic nebulization was also conducted using other alcohol–water mixtures, such as methanol–water, under comparable conditions. In these cases, a disc-like intermediate phase with clustered disk structures was observed (Fig. 4A and B). However, ethanol–water produced more reproducible and better-defined hierarchical structures and was therefore chosen as the optimal solvent system for the subsequent experiments. The introduction of ethanol lowers the dielectric constant of the solvent mixture, promoting rapid evaporation within the microdroplets and thereby enhancing supersaturation and nucleation. Under these conditions, partial hydrolysis of copper acetate monohydrate occurs in the ethanol–water (4 : 1) medium, leading to the formation of copper hydroxide acetate monohydrate as an intermediate phase. This intermediate is proposed to arise from the hydrolysis of the precursor, followed by the bridging of neighbouring Cu^{2+} centres by hydroxide ions. The confined microdroplet environment, together with the interfacial electric field, may further promote ion enrichment and accelerate precipitation.[26–29] Subsequent treatment in water facilitates further hydrolysis of

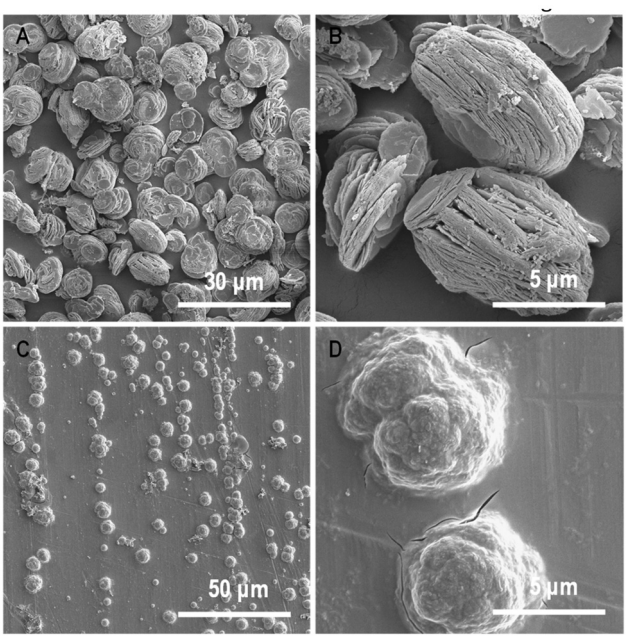

Fig. 4 (A and B) FESEM images of the intermediate formed *via* ultrasonic nebulization in MeOH : H_2O (4 : 1), exhibiting clustered disk-like structures. (C and D) FESEM images of the final product obtained after subsequent sonication of the intermediate in water, where no porous nanostructures were observed.

the intermediate, while dehydration drives its transformation into crystalline CuO. The observed disc-like morphology is attributed to evaporation-induced Marangoni flow. In multicomponent droplets, differential evaporation generates surface-tension gradients that drive internal recirculating convection, redistributing solute species and suppressing outward capillary transport, thus promoting uniform disc-shaped deposition. Notably, the reaction showed no observable progression in pure water, even after prolonged ultrasonic nebulization for up to 24 h, as evidenced by clear solutions and the absence of precipitate formation (Fig. S10). In contrast, the ethanol–water system yielded a distinct bluish-green precipitate, indicating successful intermediate formation (Fig. S11). Another interesting observation was that simply suspending the bluish-green intermediate precipitate in water at room temperature led to its slow conversion to blackish-brown tenorite over several days, confirming the thermodynamic favorability of the tenorite phase.[30–32]

Thermodynamic and kinetic considerations of phase transformation

The room-temperature transformation from copper acetate monohydrate to CuO is likely kinetically assisted by the unique microdroplet environment. Rapid evaporation from the microdroplets generates local supersaturation, which favours the precipitation of a metastable copper hydroxide acetate intermediate. This intermediate can persist transiently under confined interfacial conditions, where ion enrichment, altered solvation, and the intrinsic electric field at the gas–liquid interface may lower the activation barriers associated with hydrolysis and dehydration. Subsequent water treatment facilitates further hydrolysis of the intermediate, while dehydration provides the thermodynamic impetus for conversion to crystalline CuO. Thus, the ambient phase transformation is governed by a balance of kinetic acceleration and thermodynamic stabilization within the microdroplet interface.

Comparison of nebulization and bath sonication

To verify whether porous, flower-like structures were formed specifically under ultrasonic nebulization conditions, several control experiments were conducted. A copper acetate solution of identical concentration in the ethanol–water mixture (4 : 1 v/v) was first subjected to direct bath sonication. No visible change occurred during the initial 1 h of sonication, during which the temperature of the bulk solution was maintained below 40 °C using ice packs. Upon continued sonication for an additional hour without external cooling, the solution temperature exceeded 55 °C, and a small amount of precipitate formed. FESEM analysis of this precipitate revealed disc-like structures, like the intermediate observed under nebulization (Fig. S12). The precipitate was then separated, washed, and redispersed in water, followed by sonication for 3 h, during which the suspension gradually changed from light brown to black, yielding a product with a completely different, micrometer-sized morphology (Fig. 4C and D). These results confirm that microdroplet confinement and rapid evaporation gradients under nebulization are uniquely responsible for generating the porous, hierarchical nanostructures, distinguishing this method from conventional sonication.

Gram-scale synthesis and rapid U(VI) remediation performance

Our methodology can produce materials on a gram scale, as evidenced by the optical image in Fig. S13 of the dried, as-synthesized tenorite powder, which weighed 1.01 g. The as-synthesized CuO exhibits hierarchical porosity and a high surface area (25.63 m^2 g^{-1}, by BET), indicating strong adsorption potential (Fig. S14). Its performance was evaluated for As(III), As(V), Se(IV), U(VI), Pb(II), and Cd(II) using 100 mL of 1000 ppb solutions with 50 mg of adsorbent, achieving high removal efficiencies for all metals, with U(VI) showing the highest removal, reducing its concentration to <10 ppb (Fig. 5A). Due to its superior U(VI) uptake, subsequent studies focused on this ion. Dosage-dependent studies (5–100 mg in 100 mL, 1000 ppb U(VI)) showed that <20 mg was sufficient to lower U(VI) below 10 ppb (Fig. 5B). Kinetic studies at 1 ppm U(VI) revealed rapid adsorption, reaching <10 ppb within 5 min using 20 mg adsorbent (Fig. 5C), following pseudo-second-order kinetics (q_e = 4.67 mg g^{-1}, k = 12.12 gmg^{-1} min^{-1}). Despite modest q_e due to low loading of the initial solution, the system demonstrates strong practical potential for rapid remediation. Langmuir analysis at higher concentrations gave q_{max} = 113 mg g^{-1} (Fig. S15), comparable to oxide sorbents. Adsorption experiments with other metals including As(III), As (V), Se(IV), Pb(II), and Cd(II) indicate that the synthesized CuO is not completely non-selective, as it can remove several heavy metal species to varying extents (Fig. 5A). However, the substantially higher uptake of U(VI) suggests a clear preference of the hierarchical CuO for uranyl ions. This selectivity may be

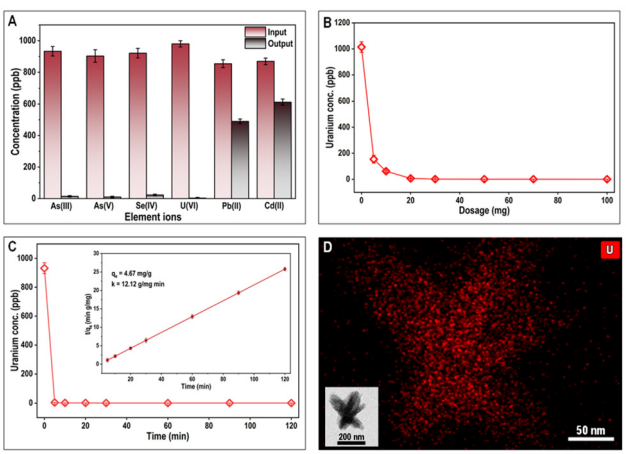

Fig. 5 Adsorption performance and post-adsorption characterization of CuO for heavy metal removal. (A) Removal efficiency for As(III), As(V), Se(IV), U(VI), Pb(II), and Cd(II) from 1000 ppb solutions. (B) Effect of adsorbent dosage (5–100 mg) on U(VI) removal efficiency. (C) Time-dependent adsorption kinetics of U(VI), showing rapid removal (<10 ppb within 5 min); inset shows the linear fitting of the pseudo-second-order kinetic model. (D) TEM-EDS elemental mapping confirming uniform uranium adsorption on the flower-like CuO nanostructures.

related to the unique coordination behavior of UO_2^{2+}, its high charge density, and its strong surface interaction with hydroxylated CuO sites. To evaluate the practical applicability of the synthesized CuO, multiple adsorption–desorption cycles were performed, and a range of regeneration eluents, including acidic, alkaline, and carbonate-based solutions, with and without an oxidizing agent, were screened. The desorption efficiency under the tested conditions remained partial and did not achieve complete regeneration; among the eluents examined, the highest desorption efficiency of approximately 50% was obtained using 1 M Na_2CO_3 + 0.2 M H_2O_2, whereas 0.1 M HNO_3 afforded 23% desorption and 0.1 M HCl caused material instability. Importantly, despite partial desorption, uranium removal performance remained consistent over successive cycles. This behaviour is attributed to the batch adsorption conditions, which were operated below the adsorbent's saturation (maximum capacity = 113 mg g^{-1}). Consequently, a substantial fraction of active sites remained available after each cycle, allowing the partially regenerated CuO to sustain comparable uranium uptake in subsequent adsorption steps. As shown in Fig. S16, the adsorbent maintained consistently high U(VI) removal efficiency throughout the reuse studies, with negligible variation in effluent U(VI) concentration and adsorption efficiency remaining above 99% over all cycles. These results confirm the stability and reusability of the hierarchical CuO adsorbent under the tested conditions, while indicating that further optimization of the regeneration protocol will be required to achieve quantitative uranium desorption. TEM-EDS confirmed uniform uranium distribution (Fig. 5D), while FESEM showed preserved morphology after multiple cycles (Fig. S17). Consistent with these observations, XRD patterns collected after U(VI) adsorption showed no discernible changes in the crystal structure of CuO (Fig. S18), indicating excellent structural stability during the adsorption process. To gain insight into the adsorption mechanism, XPS analyses of the adsorbent after U(VI) uptake were conducted, and the high-resolution spectra are shown in Fig. S19. The U 4f spectrum (Fig. S19B) exhibits characteristic U $4f_{7/2}$ and U $4f_{5/2}$ peaks at 381.7 eV and 392.5 eV, respectively, accompanied by shake-up satellite features, confirming the presence of uranium predominantly in the hexavalent oxidation state. The absence of detectable U(IV)-related components indicates that U(VI) remains largely unchanged during adsorption. These results suggest that uranium uptake occurs primarily through surface complexation and/or surface precipitation rather than through U(VI) reduction. In addition, the Cu 2p spectrum (Fig. S19A) remains consistent with the CuO framework, indicating that the adsorbent preserves its chemical integrity after adsorption.

Conclusions

In conclusion, we demonstrate a microdroplet-based strategy that enables room-temperature synthesis of porous, flower-like CuO nanostructures *via* a copper hydroxide acetate monohydrate intermediate. Unlike conventional hydrothermal/solid-state methods that require 250–600 °C and elevated pressures, ultrasonic nebulization of ethanol–water microdroplets creates confinement, rapid evaporation, and concentration gradients analogous to those in hydrothermal reactors, yielding gram-scale, phase-pure CuO under ambient conditions. Comprehensive analyses confirmed the unique role of nebulization over bulk sonication, producing hierarchical nanostructures with exceptional adsorption performance: U(VI) reduced from 1000 ppb to <10 ppb in 5 min, outperforming commercial CuO (>20-fold) while retaining morphology. The versatility of the microdroplet-assisted approach was further demonstrated through the successful synthesis of silver oxide and zinc-based intermediate phases. This energy-efficient approach eliminates high-temperature calcination, offering broad utility for oxides and surfactant-free nanoparticles *via* 'ambient hydrothermal synthesis' microdroplet mechanochemistry, bridging solution and solid-state chemistry.

Author contributions

A. N.: data collection, data analysis, data interpretation, interpretation of results, and writing the article. A. M.: SEM imaging, data analysis, data interpretation, and interpretation of results, S. S.: uranium adsorption studies, S. M.: ultrasonic nebulization, S. C.: XPS measurement, P. P.: data analysis, D. S.: conception and design of work, supervision of data collection and analysis, interpretation of results, drafting and editing of the article. T. P.: conception and design of work, supervision of data analysis, interpretation of results, writing and editing of the final version of the article.

Conflicts of interest

There are no conflicts to declare.

Data availability

The data supporting this article are included in the main article and its supplementary information (SI). Supplementary information is available. See DOI: https://doi.org/10.1039/d6nr01419d.

No additional data have been deposited in external repositories.

Acknowledgements

This work was supported by the ANRF Science and Engineering Research Board (SERB), Department of Science and Technology (DST), Government of India. T. P. acknowledges support from SERB under the SUPRA scheme (SPR/2021/000439) and a JC Bose Fellowship of Anusandhan National Research Foundation (ANRF). We acknowledge the

support of the Centre of Excellence on Molecular Materials and Functions under the institution of Eminence scheme of IIT Madras. The authors acknowledge the Department of Chemistry, IIT Madras, for carrying out the TGA, PXRD, and BET measurements. The Talos F200i microscope at ANRF National Facility for Cryo-EM, IIT Madras, was used for TEM/STEM/EDS image analysis and was gratefully acknowledged.

References

1 B. K. Spoorthi, K. Debnath, P. Basuri, A. Nagar, U. V. Waghmare and T. Pradeep, *Science*, 2024, **384**, 1012–1017.
2 D. Sarkar, M. K. Mahitha, A. Som, A. Li, M. Wleklinski, R. G. Cooks and T. Pradeep, *Adv. Mater.*, 2016, **28**, 2223–2228.
3 K. S. Aswathi, K. Unni, S. Mukhopadhyay, A. Som, S. Chowdhury, S. K. Jana, D. Sarkar and T. Pradeep, *Nanoscale Horiz.*, 2026, **11**, 1053–1062.
4 A. Mahapatra, A. Som, B. K. Spoorthi, D. Sarkar and T. Pradeep, *Chem. Commun.*, 2025, **61**, 15846–15849.
5 K. Unni, J. S. Kumar, A. Som, D. Sarkar and T. Pradeep, *ACS Sustainable Chem. Eng.*, 2024, **12**, 11957–11967.
6 D. Sarkar, A. Som, K. Unni, S. Manna and T. Pradeep, *Small*, 2025, **21**, 2400159.
7 A. Li, Z. Baird, S. Bag, D. Sarkar, A. Prabhath, T. Pradeep and R. G. Cooks, *Angew. Chem., Int. Ed.*, 2014, **53**, 12528–12531.
8 X. Yan, R. M. Bain and R. G. Cooks, *Angew. Chem., Int. Ed.*, 2016, **55**, 12960–12972.
9 J. Ghosh and R. G. Cooks, *TrAC, Trends Anal. Chem.*, 2023, **161**, 117010.
10 J. K. Lee, S. Banerjee, H. G. Nam and R. N. Zare, *Q. Rev. Biophys.*, 2015, **48**, 437–444.
11 J. K. Lee, D. Samanta, H. G. Nam and R. N. Zare, *Nat. Commun.*, 2018, **9**, 1562.
12 P. Jia, L. Rao, D. Hong, T. Wu, J. Yu, C. Yang, Y. Hu, X. Luo, W. Dou, X. Qian, H. Yang and L. Xu, *Angew. Chem., Int. Ed.*, 2026, **65**, e22301.
13 L. Rao, X. Zhang, P. Liu, W.-T. Dou, H.-Y. Lin, F. Zhao, W. Zhu, X. Qian, H.-B. Yang and L. Xu, *J. Am. Chem. Soc.*, 2025, **147**, 31618–31629.
14 D. Sarkar, A. Mahapatra, A. Som, R. Kumar, A. Nagar, A. Baidya and T. Pradeep, *Adv. Mater. Interfaces*, 2018, **5**, 1800667.
15 J. Xie, M. Xie, Y. Zhao, W. Shen, J. Li, Q. Wang, X. Yan, M. Shi, L. Chai and L. Zhang, *Chem. Commun.*, 2026, **62**, 6187–6191.
16 D. Satyabola, T. Ahuja, S. Bose, B. Mondal, P. Srikrishnarka, M. P. Kannan, B. K. Spoorthi and T. Pradeep, *J. Phys. Chem. C*, 2021, **125**, 10998–11006.
17 T. Pradeep, *ACS Sustainable Chem. Eng.*, 2026, **14**, 25–30.
18 G. Rovelli, M. I. Jacobs, M. D. Willis, R. J. Rapf, A. M. Prophet and K. R. Wilson, *Chem. Sci.*, 2020, **11**, 13026–13043.
19 A. Ray Chowdhuri, B. K. Spoorthi, B. Mondal, P. Bose, S. Bose and T. Pradeep, *Chem. Sci.*, 2021, **12**, 6370–6377.
20 D. Sarkar, R. Singh, A. Som, C. K. Manju, M. A. Ganayee, R. Adhikari and T. Pradeep, *J. Phys. Chem. C*, 2018, **122**, 17777–17783.
21 M. Outokesh, M. Hosseinpour, S. J. Ahmadi, T. Mousavand, S. Sadjadi and W. Soltanian, *Ind. Eng. Chem. Res.*, 2011, **50**, 3540–3554.
22 G. Qiu, S. Dharmarathna, Y. Zhang, N. Opembe, H. Huang and S. L. Suib, *J. Phys. Chem. C*, 2012, **116**, 468–477.
23 D. Qi, H. Behrens, M. Lazarov, R. Botcharnikov, C. Zhang, C. Ostertag-Henning and S. Weyer, *ACS Earth Space Chem.*, 2024, **8**, 499–519.
24 M. Fukuda and N. Koga, *J. Phys. Chem. C*, 2018, **122**, 12869–12879.
25 S. Asbrink and A. Waskowska, *J. Phys.: Condens. Matter*, 1991, **3**, 8173–8180.
26 H. Xiong, J. K. Lee, R. N. Zare and W. Min, *J. Phys. Chem. Lett.*, 2020, **11**, 7423–7428.
27 C. F. Chamberlayne and R. N. Zare, *J. Chem. Phys.*, 2020, **152**, 184702.
28 H. Hao, I. Leven and T. Head-Gordon, *Nat. Commun.*, 2022, **13**, 280.
29 X. Cao, S.-Y. Yang, Q.-B. Xiao and X.-W. Liu, *J. Am. Chem. Soc.*, 2025, **147**, 47489–47497.
30 G. Akerlof, *J. Am. Chem. Soc.*, 1932, **54**, 4125–4139.
31 S. Semenov, A. Trybala, H. Agogo, N. Kovalchuk, F. Ortega, R. G. Rubio, V. M. Starov and M. G. Velarde, *Langmuir*, 2013, **29**, 10028–10036.
32 Z. Wang, D. Orejon, Y. Takata and K. Sefiane, *Phys. Rep.*, 2022, **960**, 1–37.

